

Syddansk Universitet

Nanoconfined NaAlH₄ Conversion Electrodes for Li Batteries

Huen, Priscilla; Peru, Filippo; Charalambopoulou, Georgia; Steriotis, Theodore A.; Jensen, Torben R.; Ravnsbæk, Dorthe Bomholdt

Published in:
ACS Omega

DOI:
[10.1021/acsomega.7b00143](https://doi.org/10.1021/acsomega.7b00143)

Publication date:
2017

Document version
Publisher's PDF, also known as Version of record

Citation for published version (APA):
Huen, P., Peru, F., Charalambopoulou, G., Steriotis, T. A., Jensen, T. R., & Ravnsbæk, D. B. (2017). Nanoconfined NaAlH₄ Conversion Electrodes for Li Batteries. ACS Omega, 2(5), 1956-1967.
<https://doi.org/10.1021/acsomega.7b00143>

General rights

Copyright and moral rights for the publications made accessible in the public portal are retained by the authors and/or other copyright owners and it is a condition of accessing publications that users recognise and abide by the legal requirements associated with these rights.

- Users may download and print one copy of any publication from the public portal for the purpose of private study or research.
- You may not further distribute the material or use it for any profit-making activity or commercial gain
- You may freely distribute the URL identifying the publication in the public portal ?

Take down policy

If you believe that this document breaches copyright please contact us providing details, and we will remove access to the work immediately and investigate your claim.

Nanoconfined NaAlH₄ Conversion Electrodes for Li Batteries

Priscilla Huen,[†] Filippo Peru,[‡] Georgia Charalambopoulou,[‡] Theodore A. Steriotis,[‡] Torben R. Jensen,[†] and Dorthe B. Ravnbaek^{*,§,||}

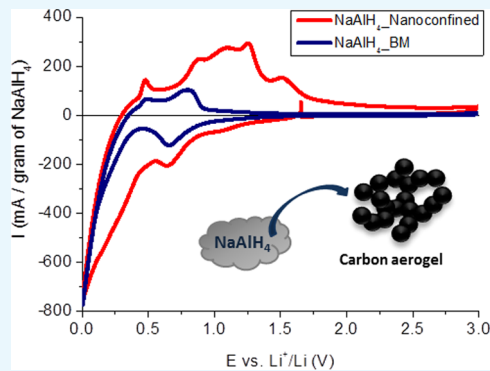
[†]Center for Materials Crystallography, Interdisciplinary Nanoscience Center and Department of Chemistry, Aarhus University, Langelandsgade 140, 8000 Aarhus C, Denmark

[‡]National Center for Scientific Research “Demokritos”, 15310 Agia Paraskevi Attikis, Greece

^{*}Department of Physics, Chemistry and Pharmacy, University of Southern Denmark, Campusvej 55, 5230 Odense M, Denmark

Supporting Information

ABSTRACT: In the past, sodium alanate, NaAlH₄, has been widely investigated for its capability to store hydrogen, and its potential for improving storage properties through nanoconfinement in carbon scaffolds has been extensively studied. NaAlH₄ has recently been considered for Li-ion storage as a conversion-type anode in Li-ion batteries. Here, NaAlH₄ nanoconfined in carbon scaffolds as an anode material for Li-ion batteries is reported for the first time. Nanoconfined NaAlH₄ was prepared by melt infiltration into mesoporous carbon scaffolds. In the first cycle, the electrochemical reversibility of nanoconfined NaAlH₄ was improved from around 30 to 70% compared to that of nonconfined NaAlH₄. Cyclic voltammetry revealed that nanoconfinement alters the conversion pathway, and operando powder X-ray diffraction showed that the conversion from NaAlH₄ into Na₃AlH₆ is favored over the formation of LiNa₂AlH₆. The electrochemical reactivity of the carbon scaffolds has also been investigated to study their contribution to the overall capacity of the electrodes.



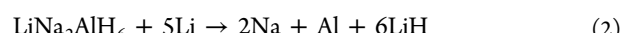
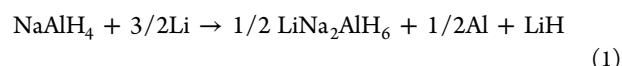
INTRODUCTION

Conversion-type electrodes are interesting alternatives to conventional intercalation electrodes for Li-ion batteries mainly due to their high capacities. In conversion-type electrodes, lithium reacts with the electrode material through a simple reaction that is generally described as follows: M_aX_b + (b·n)Li ↔ aM + bLi_nX, where M is a transition metal, X is an anion, and n is the oxidation state of X. However, this class of electrodes is still far from reaching commercial applications, as the electrodes suffer from large voltage hysteresis between the discharge and charge reactions; poor Coulombic efficiency in the first cycle; and, in many cases, poor cycling performance due to structural reorganization, particle decohesion, and phase separation.¹ Hence, design and investigation of novel conversion-type electrode materials is needed to develop upon this class of materials.

Metal hydride materials, which have previously been investigated as hydrogen storage materials for energy purposes,² are now receiving increased attention as a new class of electrode materials.³ Light-element hydrides possess higher gravimetric and volumetric energy densities than those of any known conversion-type material. The properties of magnesium hydride, MgH₂, as an electrode were first investigated by Oumellal and co-workers, and it was shown to have a high reversible capacity of 1480 mA h/g and small voltage hysteresis of ~0.2 V.⁴ The use of a metal hydride as a negative electrode of rechargeable batteries is not limited to binary metal hydride

systems; complex transition metal hydrides, Mg₂MH_x (M = Fe, Co, Ni),⁵ and lightweight alkaline alanates have also been considered.^{6–8}

Sodium alanate, NaAlH₄, has a theoretical gravimetric capacity of 1985 mA h/g. A two-step conversion lithiation reaction of NaAlH₄ is described by Latroche and co-workers, as follows⁶



The complete conversion reaction involves the exchange of four Li ions through the formation of the intermediate LiNa₂AlH₆. This reaction pathway is based on observations made by powder X-ray diffraction. Subsequently, Reale and co-workers proposed the existence of a second conversion path via Na₃AlH₆ through observations made by *in situ* powder X-ray diffraction through the following reaction⁷



The possible co-existence of two intermediates makes the electrochemical conversion of NaAlH₄ a more complicated

Received: February 8, 2017

Accepted: April 26, 2017

Published: May 10, 2017



system than typical hydride systems. However, similar to other conversion-type electrodes, NaAlH_4 also suffers from poor reversibility, which may be attributed to the large volume change and phase separation during electrochemical operation. This calls for new approaches to improve the performance of metal hydrides as conversion-type electrodes.

Nanoconfinement is a bottom-up approach wherein a material is infiltrated into a chemically inert nanoporous scaffold. This approach effectively limits the particle size to the size of the pores and cavities in the scaffold and may also reduce phase separation during chemical conversion.^{9,10} Nanoporous carbon aerogels with varying pore sizes and volumes are often used as the confining scaffolds, and a wide range of different metal hydrides have been nanoconfined, with a focus on hydrogen storage properties, for example, MgH_2 , NaAlH_4 , and reactive hydride composites, $2\text{LiBH}_4-\text{MgH}_2$.^{9,11–14} There is a strong kinetic effect for hydrogen release and uptake and a smaller “nanoeffect” for pore sizes (D) ~ 30 nm.¹⁵ One advantage of carbon aerogel scaffolds is that the surface area and pore volume can be increased by a postsynthetic treatment (heating to >600 °C in CO_2), typically referred to as activation, while maintaining a relatively constant pore size.^{16,17} Thus, relatively large amounts of active metal hydride material can be infiltrated to reach large energy densities, with potential for use in both batteries and hydrogen storage. Compared to those in nonactivated carbon aerogel, NaAlH_4 in activated-carbon aerogel shows slower kinetics but a more stable hydrogen storage capacity upon cycling.¹⁶ The carbon scaffolds are electronically conductive and also function as an effective current collector for the electrode as an intimate contact to the conversion-type metal hydride is maintained. This property is similar to that of metallic sponges, for example, Ni sponges, which are often employed in electrode fabrication.¹⁸ Moreover, the small particle size of the confined electrode material and the high surface area reduce the diffusion distances of Li ions and improve the reactivity. Nanoconfinement in mesoporous carbon has been used for improving the performances of conversion electrodes such as FeF_2 and P.^{19,20} It has been reported that MgH_2 nanoconfined in porous carbon (surface area, $S_{\text{BET}} = 500 \text{ m}^2/\text{g}$) after ball milling demonstrates good cyclic stability.²¹ These results encourage further studies for enhancing the properties of light-element metal hydride electrodes by nanoconfinement, which is the focus of the present investigations.

In this article, we report on the electrochemical performance of NaAlH_4 nanoconfined by melt infiltration in two types of conductive mesoporous carbon scaffolds that have previously been investigated in rechargeable batteries: resorcinol formaldehyde carbon aerogel^{22,23} and CMK-3.^{24–26} We show through cyclic voltammetry (CV) and operando synchrotron radiation powder X-ray diffraction (SR-PXD) that nanoconfinement alters the reaction mechanism of the lithiation process.

RESULTS AND DISCUSSION

To study the effect of nanoconfinement in different mesoporous carbon scaffolds on the electrochemical reactivity of NaAlH_4 , electrode samples of NaAlH_4 melt-infiltrated into a resorcinol formaldehyde carbon scaffold (Na_CA) and into a mesoporous carbon CMK-3 (Na_CMK3) as well as a sample of ball-milled NaAlH_4 (Na_BM) were prepared (see Table 1).

Carbon aerogel and CMK-3 were prepared by pyrolysis at a high temperature (≥ 800 °C), followed by further heat treatment. This treatment eliminates hydrogen and oxygen in

Table 1. Investigated Samples and Preparation Methods

sample	sample name	treatment
NaAlH_4	Na_BM	bulk, ball milled for 2 h
NaAlH_4	Na_CA	NaAlH_4 melt-infiltrated in activated-carbon aerogel
NaAlH_4	Na_CMK3	NaAlH_4 melt-infiltrated in heat-treated CMK-3
carbon aerogel	CA	activated in CO_2 flow for 5 h at 950 °C
CMK-3	CMK-3	heat-treated in Ar flow at 700 °C

the carbon scaffolds^{27,28} and thereby eliminates possible reactions between the scaffold and NaAlH_4 during melt infiltration. Furthermore, it is reported that carbon materials demonstrate large voltage hysteresis, and the extent of hysteresis is proportional to the hydrogen content.²⁹ Thus, removal of the H-group helps reduce hysteresis by minimizing the quasireversible binding between Li and the hydrogen-terminated edges of the scaffold.²⁸

Before infiltration, both CA and CMK-3 have surface areas of above $1000 \text{ m}^2/\text{g}$. CMK-3 has a uniform pore size of 4.7 nm, whereas CA has a broader pore size distribution, with an average diameter of 24.3 nm (see Supporting Information Figure S1). After infiltration, both the surface area and total pore volume of the carbons, as determined by N_2 adsorption measurements, decrease dramatically (see Table 2). Both CA

Table 2. Morphological Parameters of Empty and Infiltrated Carbon Scaffolds

sample	surface area S_{BET} (m^2/g)	average pore size D_{max} (nm)	total pore volume V_{tot} (cm^3/g)	NaAlH_4 (wt %) ^a	NaAlH_4 (vol %) ^b
CA	1586	24.3	2.04		
Na_CA	78	21.9	0.38	69	79
CMK-3	1162	4.7	1.20		
Na_CMK3	772	3.7	0.80	40	46

^aCalculation based on the quantity of NaAlH_4 being added for melt infiltration. ^bCalculated from the bulk density of NaAlH_4 and the total pore volume of the scaffold.

and CMK-3 comprise fully accessible and highly interconnected pore networks. In such open pore spaces, percolative blocking (e.g., due to pore mouth blocking) is highly unlikely, especially for nitrogen molecules. In this respect, the decrease in the amount adsorbed (and thus the deduced pore volume) is a very strong indication of successful NaAlH_4 infiltration.

In the case of the CA scaffold, NaAlH_4 infiltration leads to an almost 80% reduction in the initial total pore volume (from 2.04 to $0.38 \text{ cm}^3/\text{g}$), in good agreement with the theoretical vol % hydride loading (as calculated based on the actual amount of NaAlH_4 used for the infiltration and its bulk density). For Na_CMK3, the total pore volume decreases from 1.20 to $0.80 \text{ cm}^3/\text{g}$, which corresponds to a filled pore volume of 33%, lower than the theoretical loading of 46 vol %. This deviation suggests that in the case of CMK-3 a small quantity of NaAlH_4 might also reside on the external surface of the carbon particles, without, however, affecting the accessibility of the pores. Complete pore mouth blocking or infiltration failure should be ruled out, as the former would lead to zero N_2 adsorption and the latter, to no pore volume reduction for the $\text{NaAlH}_4/\text{CMK-3}$ composite.

High-angle annular dark-field (HAADF) scanning transmission electron microscopy (STEM) coupled with energy

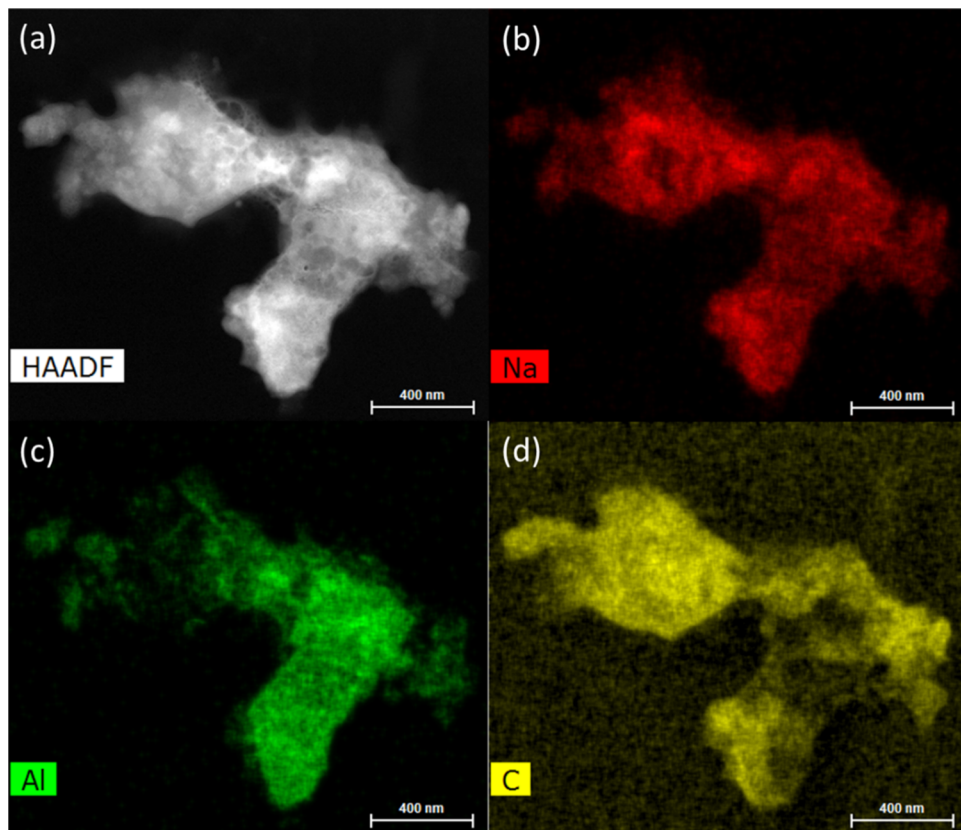


Figure 1. Representative (a) HAADF-STEM image and EDX elemental mapping images of (b) Na, (c) Al, and (d) C of Na_CA.

dispersive X-ray (EDX) elemental mapping of a CA scaffold particle containing NaAlH_4 shows that NaAlH_4 is dispersed in the CA scaffold and no significant agglomeration is observed (see Figure 1). For Na_BM, particles >150 nm in diameter were obtained by ball milling (see Supporting Information Figure S2). We note that high-resolution TEM was attempted, but the high-energy electron beam unfortunately caused the hydride to decompose. The EDX spectrum of Na_BM confirms the absence of impurities from the milling jars. Also, for Na_CA, no impurities were observed.

The PXD patterns of the as-prepared samples are shown in Figure 2a. After ball milling of the as-received NaAlH_4 (Na_BM), only diffraction from NaAlH_4 was observed, whereas in both nanoconfined samples (Na_CA and Na_CMK3) a small amount of Al was observed due to partial decomposition of NaAlH_4 during infiltration. The amount of Al in Na_CA is 3.45 wt % on the basis of Rietveld refinement. It has been reported that nanoconfined NaAlH_4 upon partial decomposition decomposes into NaH and Al directly.³⁰ Thus, the presence of the intermediate Na_3AlH_6 in Na_CMK3 suggests that some of the NaAlH_4 is not confined inside pores. Moreover, because the pore size of CMK-3 is 4.7 nm, the Bragg peaks of infiltrated NaAlH_4 would not be easily observable by PXD due to extensive peak broadening. Hence, the sharp diffraction peaks from NaAlH_4 in Na_CMK3 likely originate from noninfiltrated NaAlH_4 . In contrast, an increase in the full width at half-maximum (FWHM) (without instrumental correction) is evident in the PXD data of Na_CA after nanoconfinement; for example, it increases from 0.075° in Na_BM to 0.107° in Na_CA for the (112) peak at $2\theta = 29.6^\circ$. However, for a crystallite size of 24 nm (the average pore size), the expected FWHM (without instrumental correction) is

$\sim 0.34^\circ$. The observed FWHM corresponds to a particle size of 102 nm (corrected for instrumental broadening). Hence, by PXD, we mainly observe NaAlH_4 , which is not infiltrated into the scaffold. However, it still confirms that besides Al no crystalline impurities are observed. Moreover, it is evident that the particle size of even the surface NaAlH_4 is reduced compared to that in the ball-milled sample, Na_BM. For the nanoconfined samples, the presence of amorphous scaffolds is observed as contributions to the background signal below $2\theta \sim 35^\circ$.

Galvanostatic Test and PXD of NaAlH_4 Electrodes. In Table 3, the possible lithiation reactions of NaAlH_4 are listed, with their calculated potentials, E_{calc} versus those of Li, as reported in previous publications.^{6–8} By Nernst's law $\Delta G = -nFE_{\text{eq}}$ (where ΔG is the Gibbs free energy of the reaction, n is the number of electrons, and F is the Faraday constant); a higher equilibrium potential indicates a more negative ΔG , that is, a thermodynamically more favorable reaction.

In the first galvanostatic discharge (see Figure 3), all samples exceeded the theoretical capacity (equivalent to four Li ions). The capacity observed at around 0.75–0.82 V versus Li is likely related to the formation of a solid electrolyte interface (SEI).³² It is also known that formation of LiAl alloy may occur at a low potential (0.29–0.36 V vs Li, see Table 3). The formation of SEI and LiAl alloy contribute to the extra capacity of NaAlH_4 electrodes. The experimental potentials are generally lower than the predicted values, likely due to kinetic limitation. Moreover, thermodynamic overpotential is neglected for the estimation of potentials in the literature.

For Na_BM, the potential is relatively constant in between $x = 0.3$ and 2.2 Li equivalents. From Table 3 it is observed that conversion from NaAlH_4 to $\text{LiNa}_2\text{AlH}_6$ (reaction 1) is slightly

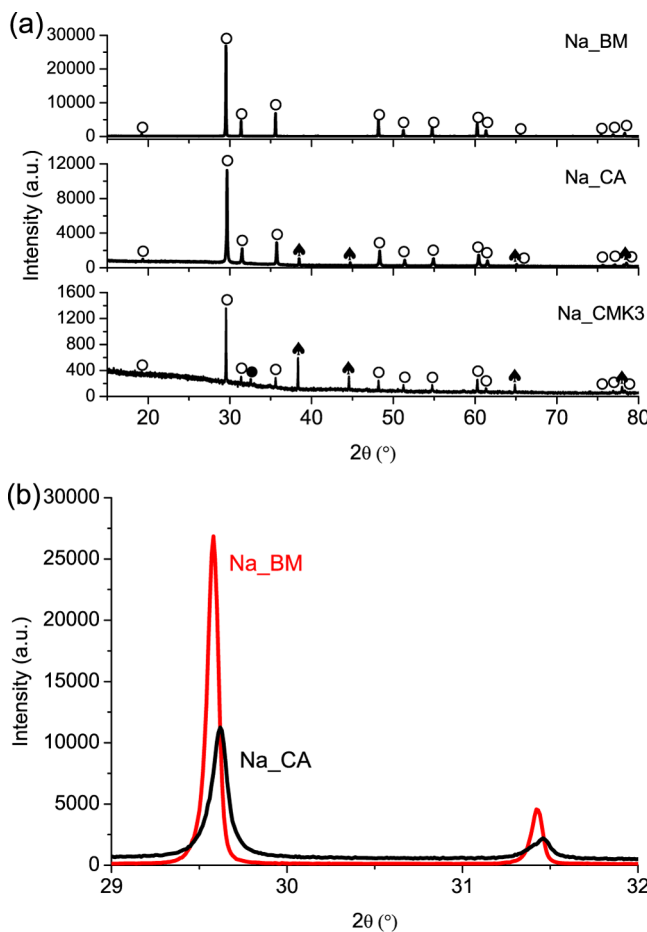


Figure 2. (a) PXD data of as-prepared Na_BM, Na_CA, and Na_CMK3. (b) PXD data of Na_BM and Na_CA from $2\theta = 29$ to 32° showing broadening of peaks ($\lambda = 1.5406 \text{ \AA}$). Symbols: ○ = NaAlH₄; “black spade suit” = Al; and ● = Na₃AlH₆.

more thermodynamically favorable than conversion to Na₃AlH₆ (reaction 3). Hence, the flat plateau of Na_BM should correspond to reaction 1. Ex situ PXD of Na_BM after the first discharge confirms that reaction 1 as well as reactions 2 and 5 take place, as diffraction peaks from LiNa₂AlH₆, Na, Al, and LiAl are observed. LiH is not observable because of the small scattering factor. There is no sign of formation of Na₃AlH₆; thus, reaction 3 does not occur in the nonconfined sample or occurs to a much smaller extent than in the nanoconfined sample. This is in accordance with the observation made by Latroche et al.⁶

In contrast to that for Na_BM, the voltage curve for Na_CA shows a more gradual slope from $x = 0.48$ to 2.0 Li equivalents in the first discharge. For Na_CA, ex situ PXD indicates that both reactions 1 and 3 occur (see Figure 4a), as weak reflection from Na₃AlH₆ is observed along reflections from LiNa₂AlH₆, Na, Al, and LiAl. Again, LiH is not observable because of the small scattering factor. The potentials of reactions 1 and 3 are very close (a difference of only 0.03 V), and these reactions may occur in parallel. Galvanostatic intermittent titrations during discharge and charge of the Na_BM and Na_CA samples (Figure 3b,c) result in relatively large voltage relaxations during 15 h under open circuit voltage conditions. For Na_BM the relaxations are in the range of 0.17–1.87 V, whereas for Na_CA, they range from 56 to 533 mV. This indicates that a large fraction of the high-voltage hysteresis between charge and discharge is due to kinetic limitations of the material. This even seems to be more severe in the ball-milled material compared with the nanoconfined material. For Na_CA, wherein around 50% recharge is achieved, a potential of 0.69 V is observed at $x(\text{Li}) = 2.75$ after relaxation, whereas during discharge, a potential of 0.43 is observed at 2.4 Li equivalents. This voltage hysteresis can be ascribed to factors affecting the thermodynamics, such as structural changes.

After the first discharge, small peaks of NaAlH₄ are found in both Na_BM and Na_CA, suggesting that the conversion is not fully complete. However conversion of NaAlH₄ to LiNa₂AlH₆ and then to metallic Na and Al is confirmed as is the formation of the LiAl alloy, which is also observed in both samples. Na₃AlH₆ is only observed during the discharge of the nanoconfined sample, Na_CA.

For Na_CMK3, the discharge–charge curve is significantly different, for example, the plateau at 0.45 V versus Li is significantly shorter than that for the other samples, and even though Na_CMK3 has a high capacity, only a small fraction seems to originate from the desired conversion reaction of NaAlH₄. As seen in Figure 4a, mainly the LiAl alloy is formed during the first discharge of Na_CMK3. The Bragg peaks at $2\theta < 23^\circ$ could be related to reactions between the material and electrolyte. Upon cycling, the discharge–charge curve of Na_CMK3 (not shown) becomes more similar to that of empty CMK-3, as reported in the literature, which shows a large hysteresis without any plateau in the charge cycle.³³ Because Na_CMK3 is not very reactive, we focus only on Na_BM and Na_CA in the following diffraction analysis.

Na_CA performs better than Na_BM in the first charge. The initial columbic efficiencies of Na_CA and Na_BM were around 70 and 30%, respectively. Both samples had a plateau at 0.43 V versus Li, which is believed to be attributed to the

Table 3. Calculated Potentials of Different Conversion Reaction Pathways As Reported in the Literature^a

reaction	E_{calc} (V vs Li)	references
NaAlH ₄ + 3/2Li \rightleftharpoons 1/2LiNa ₂ AlH ₆ + 1/2Al + LiH	0.73–0.76	refs 6 and 7
LiNa ₂ AlH ₆ + 5Li \rightleftharpoons 2Na + Al + 6LiH	0.54–0.56	refs 6 and 7
NaAlH ₄ + 2Li \rightleftharpoons 1/3Na ₃ AlH ₆ + 2/3Al + 2LiH	0.70–0.72 ^b	ref 7
Na ₃ AlH ₆ + 6Li \rightleftharpoons 3Na + Al + 6LiH (4)	0.52 ^b –0.53	ref 7
Li + Al \rightleftharpoons LiAl (5)	0.29–0.36	refs 6 and 8

^aNote: values for reactions 3 and 4 (marked by “b”) are also calculated herein. ^bCalculated from the reported Gibbs free energy of formation of the compounds³¹ (taking reaction 3, NaAlH₄ + 2Li \rightleftharpoons 1/3Na₃AlH₆ + 2/3Al + 2LiH, as an example, the ΔG of the reaction is equals to $1/3\Delta G(\text{Na}_3\text{AlH}_6) + 2\Delta G(\text{LiH}) - \Delta G(\text{NaAlH}_4) = 1/3(-116.23) + 2(-69.96) - (-39.43) = -139 \text{ kJ/mol}$) and converted to the potential by $\Delta G = -nFE_{\text{eq}}$.

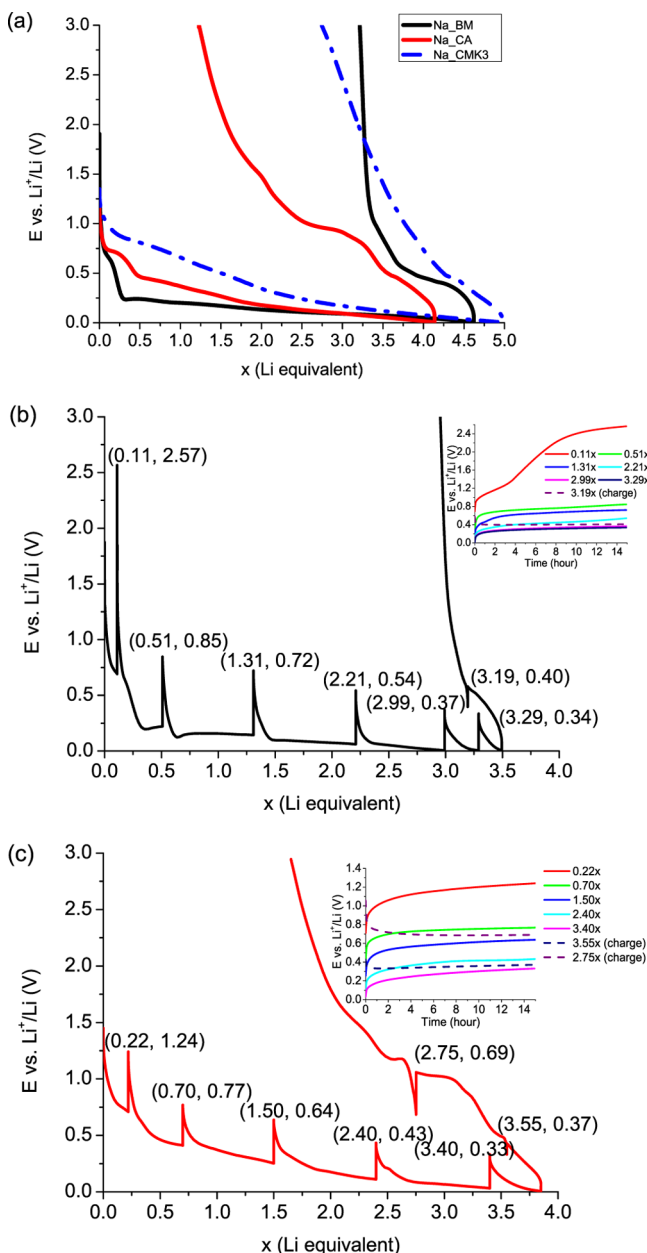


Figure 3. (a) Electrochemical performances of the sodium alanate samples in the first discharge–charge cycle at a current rate of C/10, and galvanostatic intermittent titration technique (GITT) data of (b) Na_BM and (c) Na_CA at a rate of C/10. Inset: potential vs. time of relaxation of the sample. The Li equivalent for all data is calculated using only the mass of sodium alanate.

delithiation of Al. When the charge continued, Na_CA had a second plateau at around 0.9 V versus Li and a small plateau at 1.6 V versus Li. The two plateaus are attributed to the reformation of the intermediates and NaAlH₄. This interpretation is supported by the PXD pattern of recharged Na_CA (see Figure 4b).

As Na_BM and Na_CA are recharged, the Bragg peaks of the LiAl alloy disappear. This is consistent with the delithiation of Al observed at 0.43 V versus Li in the galvanostatic test. According to the galvanostatic charge data, neither of the samples is fully reversible, and reflections from Na and Al are observed in PXD (Figures 4b). The observation of Na in the recharged state of Na_BM and Na_CA is in contrast to the

findings in Reale's work, wherein Na is absent.⁷ In Reale's work, sodium stripping is suggested to be a reason for capacity loss. Instead, the irreversibility could be due to poor diffusion of hydride, which leads to inefficient conversion from Na, Al, and LiH. In Na_BM, LiNa₂AlH₆ is converted back to NaAlH₄ partially. In Na_CA, both intermediates, LiNa₂AlH₆ and Na₃AlH₆, are fully reconverted to NaAlH₄, which is in agreement with the increased reversibility of Na_CA compared to that of Na_BM, as observed in the galvanostatic test. Hence, the data suggest that for Na_CA the reversibility of reactions 1 and 3 is increased, whereas reactions 2 and 4 limit the reversibility in both cases.

CV. The electrochemical reactions occurring in the NaAlH₄ samples and empty scaffolds were further examined using CV, see Figure 5. In the first cycle, a peak appeared at 0.64–0.68 V versus Li for all samples. This peak corresponds to the formation of SEI and it becomes negligible from the second cycle. Empty scaffolds have a larger current response for the formation of SEI than infiltrated scaffolds. This is most likely because infiltration reduces the surface area of the samples significantly (see Table 2) and results in less interaction between the scaffold and electrolyte. Differences in the surface chemistry may also play a role; however, because the infiltration process is unlikely to induce significant changes in the surface groups of the carbon scaffold, changes in the surface area is a more likely explanation.

During the first cycle of Na_BM, the sharp signal at a low potential (<0.35 V vs Li) is attributed to the lithiation of Al from reduction of the alanate. When the scan is reversed, delithiation of Al is observed at around 0.5 V versus Li and reformation of LiNa₂AlH₆, at 0.8 V versus Li. The magnitude of each current response decreases in the subsequent cycles. There is little change in the voltammogram after the fifth cycle. Interestingly, Na_CA acts differently within the same potential range. More peaks are observed from 0.65 to 1.8 V versus Li in the reverse scan, meaning more reactions take place (see Figure 5b). In contrast to Na_BM, Na_CA has a broad peak at a potential below 0.5 V versus Li, which is also observed in the voltammogram of empty CA (see Figure 5c). Intercalation of Li into carbon can happen at a low potential close to 0 V versus Li.^{29,34,35} Therefore, the broadening of the peak may correspond to the intercalation of Li into CA. When CA was scanned from 0.005 to 3.0 V versus Li, very limited current response was observed, and no significant reactions take place during the charge cycle. Hence, the peaks observed in Na_CA are solely related to the reactivity of NaAlH₄ and its intermediates. In the second cycle, only three broad peaks remain, suggesting poor to no reversibility of these reactions in Na_CA. In the fifth cycle, the only remaining peak at 0.5 V versus Li is associated with delithiation of Al. Similar to that in the published results, the LiAl alloy here has an unsatisfactory long-term stability and becomes irreversible.^{36,37} After 10 cycles, Na_CA acts similar to empty CA. According to the voltammogram of Na_CA, the origin of capacity can be divided into three parts upon cycling. The system is dominated by the conversion of NaAlH₄ → the lithiation/delithiation of Al → carbon scaffold.

For Na_CMK3, CV also shows broadening of the peak at a potential below 0.42 V versus Li. In the reverse scan, the delithiation of Al is more intense than that for Na_BM. Because of partial decomposition of NaAlH₄ during melt infiltration, Na_CMK3 already contains Al before characterization. Hence, more LiAl alloy can be formed electrochemically. This is also

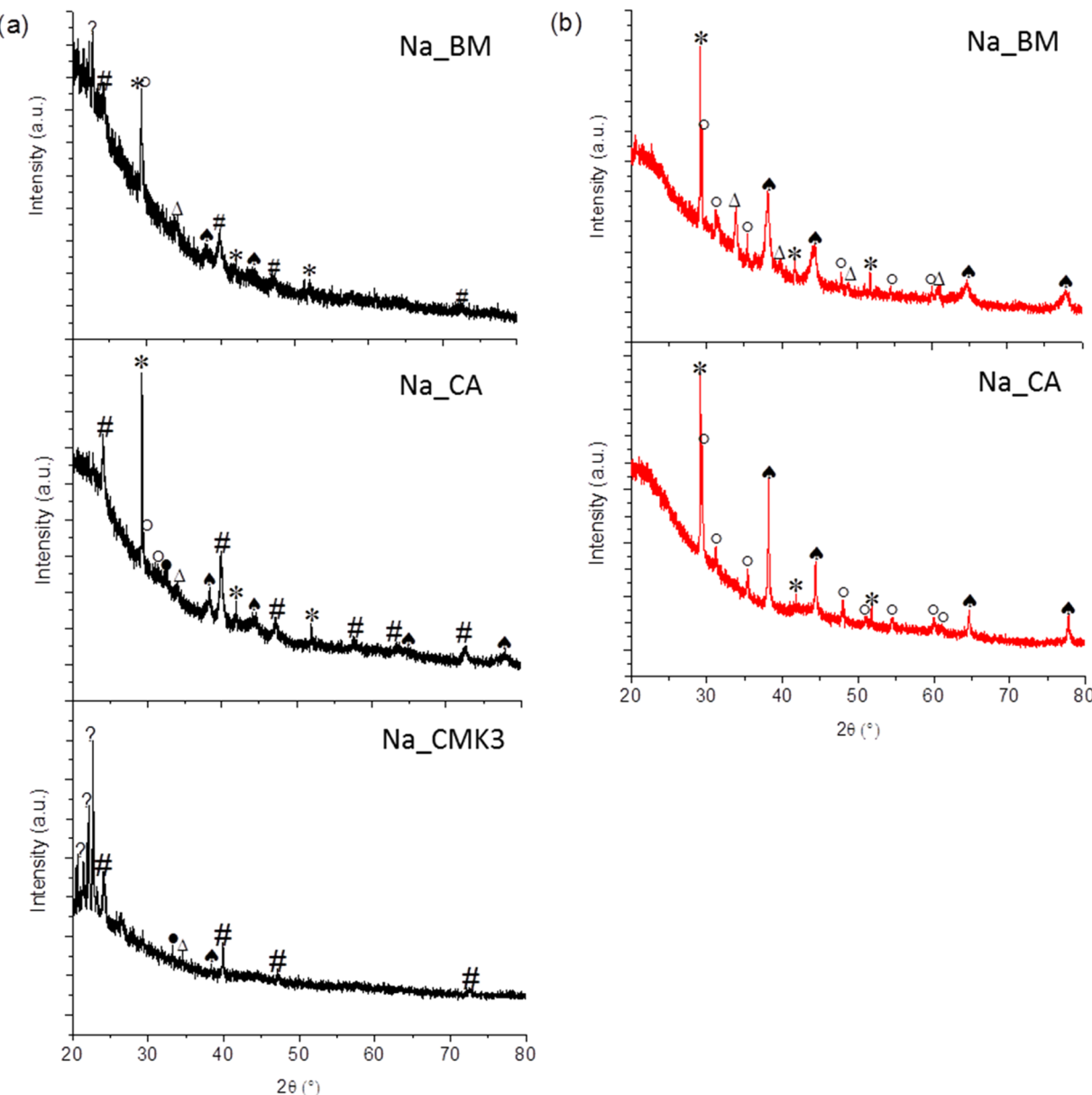


Figure 4. PXD data of (a) Na_BM, Na_CA, and Na_CMK3 after the first discharge and (b) Na_BM and Na_CA after recharging. All data are measured at room temperature (RT) ($\lambda = 1.5406 \text{ \AA}$). Symbols: ○, NaAlH₄; Δ, LiNa₂AlH₆; ●, Na₃AlH₆; “black spade suit”, Al; *, Na; #, LiAl.

observed in Na_CA. There is another small peak at 0.89 V versus Li in Na_CMK3, but it is not reversible.

From the CV results of infiltrated and empty carbon scaffolds, it is found that the reactivity of nanoconfined NaAlH₄ is not a simple sum of the data measured separately for nonconfined NaAlH₄ and the empty carbon scaffold. Nanoconfinement changes the reaction mechanism. However, the peaks in the voltammograms are heavily overlapped and it is difficult to distinguish each reaction step. To acquire more information on the reaction mechanism, the samples were investigated by operando SR-PXD.

Operando SR-PXD Studies. Figure 6 shows the operando SR-PXD data of Na_BM and Na_CA stacked as a function of Li uptake, x . As the conversion of NaAlH₄ is not complete in the operando SR-PXD study (for both samples, less than 2.4 Li equivalents was exchanged), we focus on the qualitative information, as the data provide very useful information for understanding the effect of nanoconfinement and the presence

of the carbon scaffold on NaAlH₄. The lower capacity observed in these experiments is due to the higher internal resistance of the operando cell compared to that of a normal coin cell, resulting in a larger overpotential and the lower potential limit being reached at a lower state of discharge, that is, at lower $x(\text{Li})$ -values.

Before discharging (at $x(\text{Li}) = 0.0$), both samples contain Al, which is either from partial decomposition of NaAlH₄ or the Al-foil current collector in the operando battery cell. For Na_BM, the conversion of NaAlH₄ to LiNa₂AlH₆ is initiated at $x(\text{Li}) = 0.27$, as expected. The intensity of LiNa₂AlH₆ increases continuously up to $x(\text{Li}) = 1.43$. A fraction of the LiNa₂AlH₆ may decompose into Na, Al, and LiH with time, as demonstrated by the slightly decreasing intensity of LiNa₂AlH₆ as well as the increasing intensity of Na and Al. In contrast to the ex situ PXD result, Na₃AlH₆ also forms in Na_BM. The formation of Na₃AlH₆ initiates at a deeper discharge state of $x(\text{Li}) = 1.07$. This result is consistent with the reaction

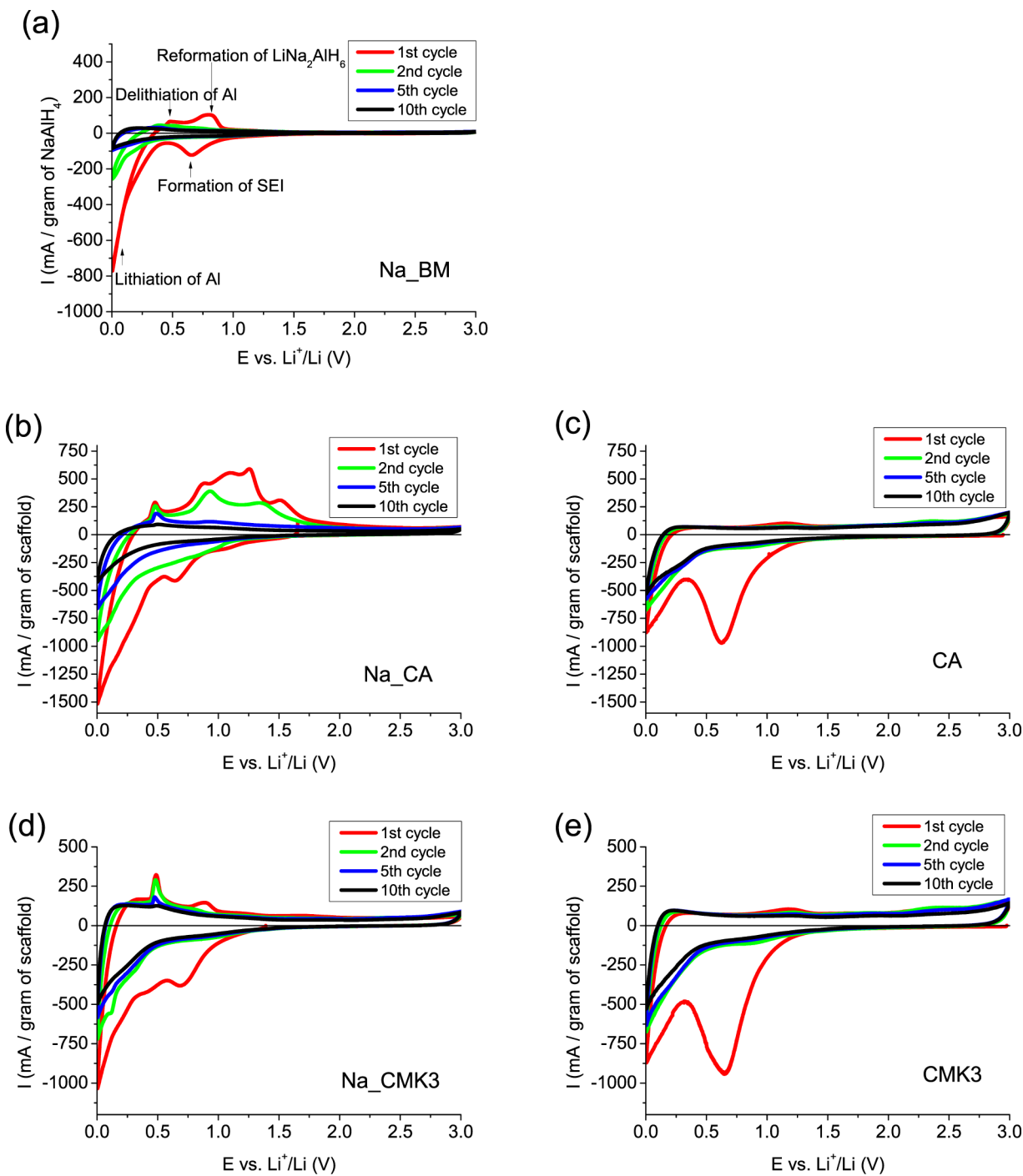


Figure 5. Cyclic voltammograms of (a) Na_BM, (b) Na_CA, (c) CA, (d) Na_CMK3, and (e) CMK-3 at a scan rate of 0.1 mV/s.

mechanism proposed by Reale et al.⁷ As mentioned previously, the conversion from NaAlH₄ to Na₃AlH₆ is less favorable and a smaller amount of Na₃AlH₆ is formed compared to that of LiNa₂AlH₆. The small amount of Na₃AlH₆ and poor resolution of the ex situ PXD pattern may explain why Na₃AlH₆ is not found in the ex situ PXD pattern (Figure 4a).

For Na_CA, the first conversion step is again the conversion to LiNa₂AlH₆ occurring at $x(\text{Li}) = 0.57$. Shortly after the formation of LiNa₂AlH₆, the formation of Na₃AlH₆ is also initiated, at $x(\text{Li}) = 0.63$. Hence, the use of the carbon scaffold seems to favor the conversion to Na₃AlH₆, which is in accordance with the observations made by ex situ PXD.

Compared to that in Na_BM, there is less LiNa₂AlH₆ present in Na_CA. As shown in Figure 6b, conversion to LiNa₂AlH₆ and Na₃AlH₆ occurs in parallel. This indicates that the conversions to LiNa₂AlH₆ and Na₃AlH₆ are competing reactions. It is believed that alteration of the reaction mechanism is most probably due to a kinetic factor because thermodynamic effects are only expected when the particle size is smaller than 2–3 nm.³⁰

Cycling Stability. In the ex situ PXD of Na_BM and Na_CA after 20 discharge–charge cycles, mainly Na, Al, and the LiAl alloy are present (see Figure 7). The PXD patterns indicate that conversion to NaAlH₄ or any intermediate

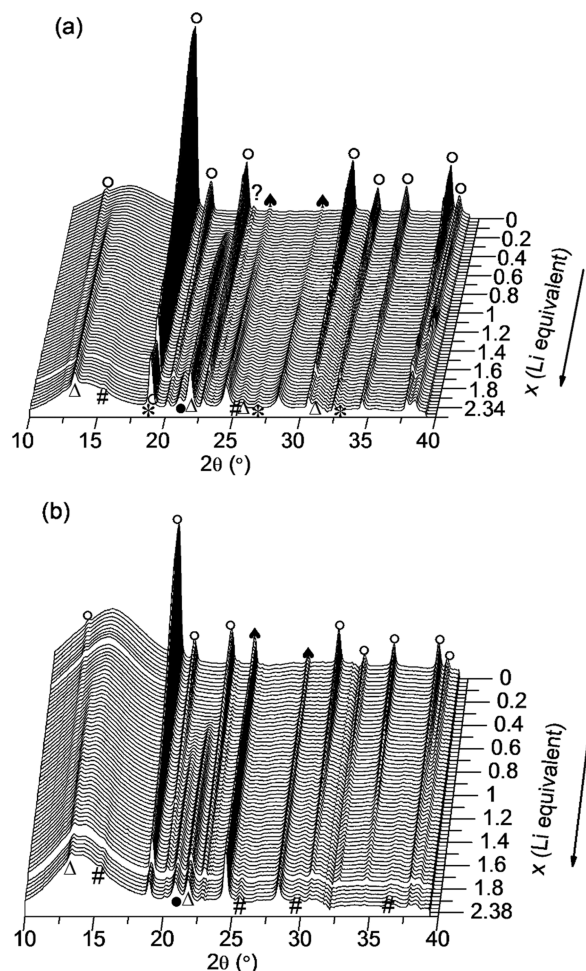


Figure 6. Operando PXD patterns of the first discharge of (a) Na_{BM} and (b) Na_{CA} measured at MAXII beamline I711 ($\lambda = 0.9940 \text{ \AA}$) using a galvanostatic current rate of C/20 and a cutoff potential of 0.005 V. Symbols: ○, NaAlH₄; Δ, LiNa₂AlH₆; ●, Na₃AlH₆; *, Al; #, LiAl; ?, Li (foil); “black spade suit”, Al (note that the Al peaks in the beginning of the experiments originate either fully (Na_{BM}) or partly (Na_{CA}) from the Al-foil current collector).

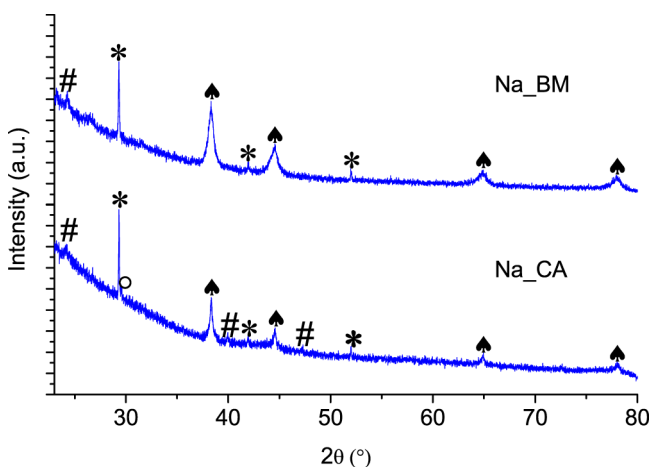


Figure 7. PXD data of Na_{BM} and Na_{CA} after 20 discharge-charge cycles measured at RT ($\lambda = 1.5406 \text{ \AA}$). Symbols: ○, NaAlH₄; “black spade suit”, Al; *, Na; #, LiAl.

becomes difficult after repeated cycles. The capacities (mA h/g of NaAlH₄) of the three NaAlH₄ samples in the first 20 cycles

are plotted in Figure 8a. Generally, all samples show a significant fall in capacity between the first and second cycles. One of the reasons of the rapid decrease in capacity is due to the formation of SEI. However, nanoconfinement in the carbon scaffold increases the capacity retention from around 23% (Na_{BM}) to 43% (Na_{CA}) and 46% (Na_{CMK3}). After 20 discharge-charge cycles, Na_{CMK3} has the highest capacity, while Na_{BM} has the lowest capacity.

From the previous sections, it is evident that the reversibility of NaAlH₄ diminishes gradually. As the carbon scaffolds are found to be electrochemically active, it is important to access their contribution toward the overall capacity of the electrodes.

Electrodes of Na_{CA} and CA containing the same amount of carbon scaffold (0.9 mg) were tested by galvanostatic discharge-charge cycling. Na_{CA} was cycled at a rate of C/10 on the basis of the amount of NaAlH₄, and the same current was applied to CA. Na_{CA} has a higher capacity than that of CA during the first five cycles, whereas the opposite is observed for the subsequent cycles (see Figure 8b). The higher capacity of Na_{CA} during the initial five cycles is due to the reactivity of NaAlH₄.

After 20 cycles, CA has a capacity of 0.70 mA h, which is equal to 773 mA h/g CA with a Coulombic efficiency of 95.6%. Interestingly, although the Coulombic efficiency is not very high, the capacity of CA is significantly higher than the capacity of graphite (372 mA h/g).³⁸ Na_{CMK3} was also compared with CMK-3. The capacity of CMK-3 is higher than that of Na_{CMK3} in all cycles, and it retains 548 mA h/g of CMK-3 after 20 cycles. From Figures 8b,c, it is clear that carbon scaffolds contribute to the overall reversible capacity, as is also revealed from the results of CV.

CONCLUSIONS

We have presented the electrochemical performance and electrochemically driven conversion mechanism of the NaAlH₄ anode nanoconfined in mesoporous carbon scaffolds. The initial Coulombic efficiency of NaAlH₄ confined in activated-carbon aerogel is at least twice that of ball-milled NaAlH₄. Using the activated-carbon aerogel also improves the kinetics of the conversion from NaAlH₄ to Na₃AlH₆ and thereby seems to alter the conversion mechanism. However, it has been found that the capacity of nanoconfined NaAlH₄ is initially dominated by the reactivity of the NaAlH₄ and LiAl alloys but later by the carbon scaffold. The loss in the reactivity of NaAlH₄ could be related to inefficient diffusion of the hydride, which may limit the extent of hydride conversion.

Nanoconfinement is a promising route for improving hydride electrodes; however, research on nanoconfinement is still at a preliminary stage and many aspects have to be considered. To enhance the reactivity of nanoconfined hydride, it is important to maximize the loading of hydride inside the scaffold, which will also increase the material capacity. It is also interesting to study the influence of pore size and different activation methods on the electrochemical reactivity of the carbon scaffold. A smaller pore size of the scaffold is expected to enhance the kinetics of the material and may also reduce polarization of the electrode. New electrically conductive but inert scaffolds may also need to be explored to understand the nanoconfinement effect in more detail.

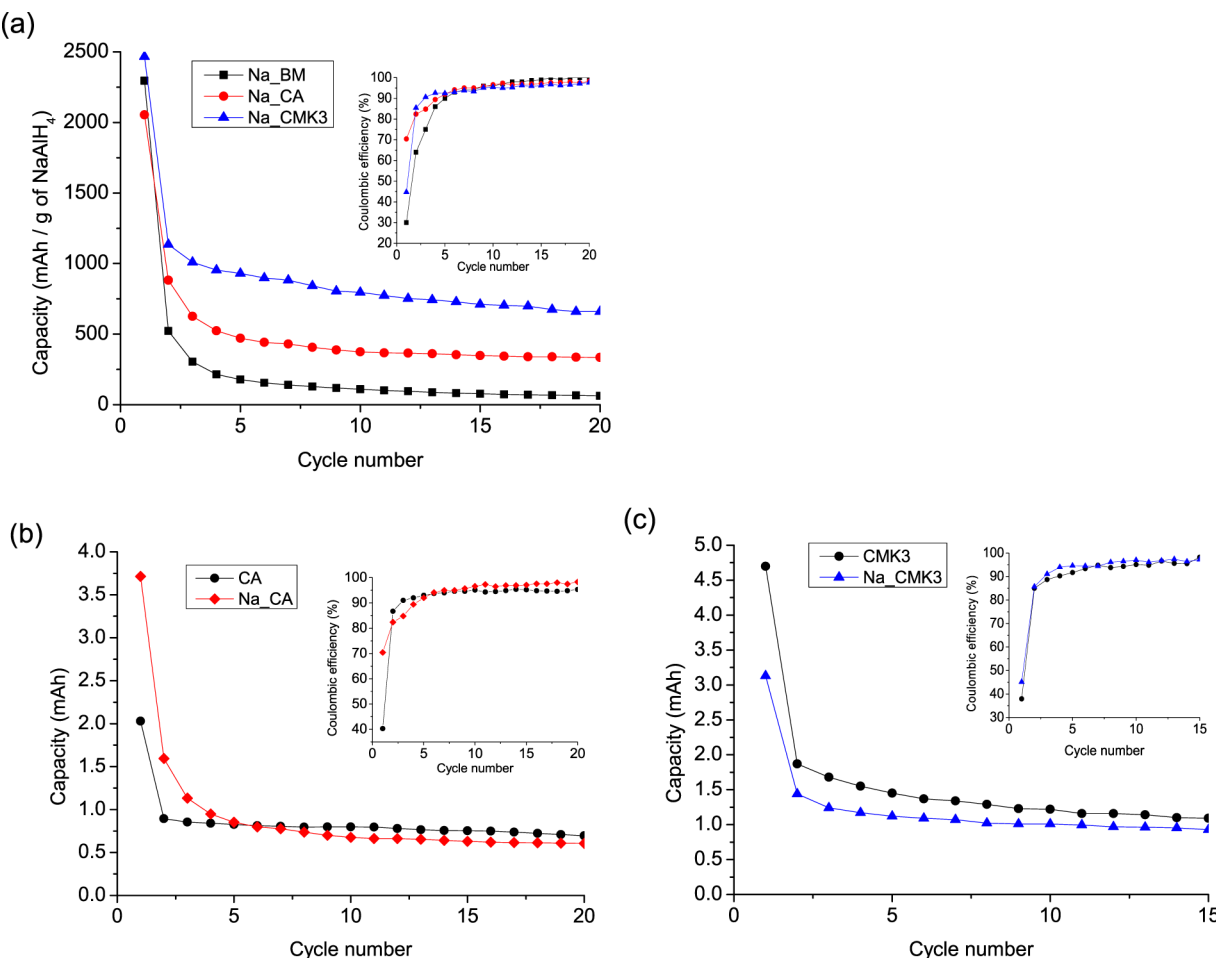


Figure 8. (a) Specific capacity of the sodium alanate samples at rate C/10 relative to the mass of NaAlH₄ (mA h/g of NaAlH₄). (b) Capacity of Na_CA vs that of empty CA under the same applied current. (c) Capacity of Na_CMK3 versus that of empty CMK-3 under the same applied current. Insets: Coulombic efficiency of the corresponding measurements.

METHODS

Apart from the synthesis of the carbon scaffolds (resorcinol formaldehyde carbon aerogel and CMK-3), all sample preparations and handling were carried out in an argon-filled glovebox equipped with a circulation purification system. The O₂ and H₂O levels were below 1 ppm at all times.

Synthesis of Carbon Aerogel. Resorcinol formaldehyde carbon aerogel was prepared by mixing resorcinol ($\geq 99.0\%$; Sigma-Aldrich), formaldehyde (37 wt % in H₂O, stabilized by 10–15% methanol; Sigma-Aldrich), and Na₂CO₃ (99.999%; Aldrich) in deionized water. The molar ratio was 1:2:8:0.0008 resorcinol/formaldehyde/H₂O/Na₂CO₃. In general, for the synthesis of the scaffold, the procedures described in refs 11 and 39 were used. Herein, the mixture was aged at RT for 24 h, at 50 °C for 24 h, and at 90 °C for 72 h. After cooling, the carbon aerogel was soaked in excess acetone. Finally, the carbon aerogel was pyrolysed at 800 °C ($\Delta T/\Delta t = 3\text{ }^{\circ}\text{C}/\text{min}$) under N₂ flow for 6 h. The surface area and total pore volume of the carbon aerogel was increased by heating the aerogel to 950 °C ($\Delta T/\Delta t = 6\text{ }^{\circ}\text{C}/\text{min}$) in a constant CO₂ flow for 5 h according to the procedure described in ref 17. This procedure denoted activation of the resorcinol formaldehyde carbon scaffold, and henceforth, this scaffold is denoted as CA. The increased surface area and total pore volume would enhance the infiltration of NaAlH₄.¹⁶

Synthesis of CMK-3. The CMK-3-type carbon scaffold was synthesized using a well-established nanocasting route, as described in ref 40, using SBA-15, a two-dimensional hexagonally ordered mesoporous silica, as the template. The SBA-15 template was also prepared for this purpose by adopting a standard surfactant-templating method, as described in ref 41. The synthesized SBA-15 silica template was infiltrated with a solution of sucrose and sulfuric acid, carbonized by pyrolysis up to 900 °C under N₂ flow, and finally washed with HF at RT to remove the silica. The as-prepared CMK-3 mesoporous carbon was further heat-treated in a tubular furnace up to 700 °C under Ar flow to remove any residual oxygen-containing groups produced on the carbon surface during the synthetic steps. The sample obtained by this thermal treatment is denoted as CMK-3.

Preparation of Nanoconfined and Ball-Milled NaAlH₄. Prior to melt infiltration, the carbon scaffolds, CA and CMK-3, were degassed in vacuum at 350 °C for several hours. For melt infiltration, NaAlH₄ (93%; Aldrich) and the degassed scaffold were added to a Swagelok-type autoclave inside an Ar-filled glovebox. To avoid decomposition of NaAlH₄, melt infiltration was performed at $p(\text{H}_2) = 210\text{--}230\text{ bar}$.¹⁵ The mixture was heated to 195 °C ($\Delta T/\Delta t = 2\text{ }^{\circ}\text{C}/\text{min}$) and dwelled for 15 min; it was then cooled to RT. These samples are denoted as Na_CA and Na_CMK3.

The reactivity of as-received NaAlH₄ was improved by ball milling for 2 h (5 min milling, 2 min pause, and 24 repetitions) using a Fritsch Pulverisette No. 6 with a speed of 350 rpm. The milling was performed in an 80 mL tungsten carbide (WC) vial using 10 mm WC balls and a ball-to-powder mass ratio of approximately 30:1. This sample of NaAlH₄ is denoted as Na_BM.

Surface Area and Pore Size Determination. The pore properties of the CA and CMK-3 scaffolds and composites before and after melt infiltration of NaAlH₄ were deduced from N₂ adsorption/desorption measurements at 77 K using a Nova 2200e surface area and pore size analyzer (Quantachrome Instruments). The surface area (S_{BET}) was determined by the Brunauer–Emmett–Teller (BET) method, whereas the mean pore size (D_{max}) was obtained from the desorption isotherm by the Barrett–Joyner–Halenda method. The total pore volume (V_{tot}) was calculated from the amount of N₂ adsorbed at $p/p_0 = 0.98$ (by assuming an adsorbate density of 0.807 g/cm³).

EDX Spectroscopy. The composition of the prepared samples, Na_BM and Na_CA, was characterized using an FEI Talos F200X scanning/transmission electron microscope with a HAADF detector and EDX system. Powders of the samples were added to anhydrous cyclohexane (99.5%; Sigma-Aldrich) and a few drops of the suspension were spread onto the copper grid. The sample grids were placed on a sample holder and transferred into the chamber in air; hence, the samples were oxidized partially prior to measurements.

Electrochemical Test. Coin cells (CR2032) were assembled in an Ar-filled glovebox. The working electrodes were prepared by thoroughly grinding the samples with acetylene black (Cabot Corporation) and carboxymethyl cellulose (CMC) (SAFT) powders in a 3:1:1 mass ratio. Prior to mixing, the CMC binder and acetylene black were degassed in vacuum at 80 °C overnight. In each cell, 3–6 mg of the electrode mixture was used in the powdered form. The working electrode was separated from the ~100 μm thick Li metal (99.9%; Aldrich) counter electrode by a piece of Whatman borosilicate glass-fiber filter paper infused with 1 M LiPF₆ in 1:1 ethylene carbonate (EC)/dimethyl carbonate (DMC) (99.9%, H₂O content <20 ppm; Solvionic).

The electrochemical tests were carried out using a Bio-Logic MPG2 multichannel battery cycler. For the galvanostatic discharge–charge tests, the coin cells were cycled in a potential window between 0.005 and 3.0 V versus Li at a current rate of C/10. When carrying out GITT, a C/10 rate was used, and the relaxation time of each step was 15 h. For calculation of the theoretical cell capacity (and thus the current rate), NaAlH₄ was considered as the only active material. For CV, the cells were scanned from the open circuit potential to 0.005 V versus Li and then reversed to 3.0 V versus Li. The rate of scanning was 0.1 mV/s for all samples.

PXD. The as-prepared samples and electrodes at selected discharge–charge states were characterized by PXD using a Rigaku SmartLab diffractometer (Cu K α_1 radiation, $\lambda = 1.5406 \text{ \AA}$) with transmission geometry. The measurements were conducted with an angular step of 3° per minute. All samples were mounted in 0.5 mm diameter Lindemann glass capillaries. For the electrode samples, coin cells were disassembled after the electrochemical tests and electrode powders were removed, ground, and mounted in capillaries inside an Ar-filled glovebox.

Operando SR-PXD was performed using electrochemical test cells of the AMPIX cell-type,⁴² which is specially designed for transmission synchrotron studies of electrochemically driven

reactions. Approximately 4–6 mg of electrode materials were mounted in the cells in an Ar-filled glovebox using ~100 μm thick Li metal foil as the counter electrode and a microporous glass-fiber separator (Whatman GF/B) with 1 M LiPF₆ in 1:1 EC/DMC as the liquid electrolyte. A piece of aluminum foil (thickness ~0.011 mm) was placed behind the working electrode to ensure uniform conductivity. The operando SR-PXD data were collected at beamline I711, MAXII in Lund, Sweden, using a selected wavelength of $\lambda = 0.9940 \text{ \AA}$. Diffraction patterns were collected in transmission geometry every 10 min with 45 s of exposure time using a large-area CCD detector. During collection of the SR-PXD data, the cell was galvanostatically discharged using a current rate of C/20 and a cutoff potential of 0.005 V versus Li.

The collected diffraction patterns were integrated using the Fit2D software.⁴³ Rietveld refinement of selected diffraction patterns was performed using Fullprof suite software.⁴⁴ The shape of the diffraction peaks was described by the pseudo-Voigt profile function, whereas the background was refined using linear interpolation between selected points.

ASSOCIATED CONTENT

Supporting Information

The Supporting Information is available free of charge on the ACS Publications website at DOI: [10.1021/acsomega.7b00143](https://doi.org/10.1021/acsomega.7b00143).

Pore size distributions of the carbon scaffolds (CA and CMK-3); HAADF-STEM images and EDX elemental mapping of the ball-milled NaAlH₄ sample (Na_BM); EDX elemental mapping of nanoconfined NaAlH₄ (Na_CA) (PDF)

AUTHOR INFORMATION

Corresponding Author

*E-mail: dbra@sdu.dk.

ORCID

Torben R. Jensen: [0000-0002-4278-3221](https://orcid.org/0000-0002-4278-3221)

Dorthe B. Ravnsbæk: [0000-0002-8172-3985](https://orcid.org/0000-0002-8172-3985)

Notes

The authors declare no competing financial interest.

ACKNOWLEDGMENTS

The technical assistance from Aref Mamakhel for EDX is gratefully acknowledged. This research has received funding from the European Marie Curie Actions under ECOSTORE grant agreement No. 607040. The work was supported by the Danish National Research Foundation, Center for Materials Crystallography (DNRF93), the Innovation Fund Denmark (project HyFill-Fast), and by the Danish Research Council for Nature and Universe (Danscatt). We are grateful to the Carlsberg Foundation. DBR thanks the Villum Foundation and the Danish Council for Independent Research for funding.

REFERENCES

- (1) Cabana, J.; Monconduit, L.; Larcher, D.; Palacín, M. R. Beyond Intercalation-Based Li-Ion Batteries: The State of the Art and Challenges of Electrode Materials Reacting Through Conversion Reactions. *Adv. Mater.* **2010**, *22*, E170–E192.
- (2) Ley, M. B.; Jepsen, L. H.; Lee, Y.-S.; Cho, Y. W.; Bellostas von Colbe, J. M.; Dornheim, M.; Rokni, M.; Jensen, J. O.; Sloth, M.; Filinchuk, Y.; et al. Complex Hydrides for Hydrogen Storage – New Perspectives. *Mater. Today* **2014**, *17*, 122–128.

- (3) Sartori, S.; Cuevas, F.; Latroche, M. Metal Hydrides Used as Negative Electrode Materials for Li-Ion Batteries. *Appl. Phys. A: Mater. Sci. Process.* **2016**, *122*, 135.
- (4) Oumella, Y.; Rougier, A.; Nazri, G. A.; Tarascon, J.-M.; Aymard, L. Metal Hydrides for Lithium-Ion Batteries. *Nat. Mater.* **2008**, *7*, 916–921.
- (5) Zaïdi, W.; Bonnet, J.-P.; Zhang, J.; Cuevas, F.; Latroche, M.; Couillaud, S.; Bobet, J.-L.; Sougrati, M. T.; Jumas, J.-C.; Aymard, L. Reactivity of Complex Hydrides Mg₂FeH₆, Mg₂CoH₅ and Mg₂NiH₄ with Lithium Ion: Far from Equilibrium Electrochemically Driven Conversion Reactions. *Int. J. Hydrogen Energy* **2013**, *38*, 4798–4808.
- (6) Teprovich, J. A.; Zhang, J.; Colón-Mercado, H.; Cuevas, F.; Peters, B.; Greenway, S.; Zidan, R.; Latroche, M. Li-Driven Electrochemical Conversion Reaction of AlH₃, LiAlH₄, and NaAlH₄. *J. Phys. Chem. C* **2015**, *119*, 4666–4674.
- (7) Silvestri, L.; Farina, L.; Meggiolaro, D.; Panero, S.; Padella, F.; Brutti, S.; Reale, P. Reactivity of Sodium Alanates in Lithium Batteries. *J. Phys. Chem. C* **2015**, *119*, 28766–28775.
- (8) Silvestri, L.; Forgia, S.; Farina, L.; Meggiolaro, D.; Panero, S.; La Barbera, A.; Brutti, S.; Reale, P. Lithium Alanates as Negative Electrodes in Lithium-Ion Batteries. *ChemElectroChem* **2015**, *2*, 877–886.
- (9) Nielsen, T. K.; Besenbacher, F.; Jensen, T. R. Nanoconfined Hydrides for Energy Storage. *Nanoscale* **2011**, *3*, 2086–2098.
- (10) de Jongh, P. E.; Adelhelm, P. Nanosizing and Nanoconfinement: New Strategies Towards Meeting Hydrogen Storage Goals. *ChemSusChem* **2010**, *3*, 1332–1348.
- (11) Nielsen, T. K.; Manickam, K.; Hirscher, M.; Besenbacher, F.; Jensen, T. R. Confinement of MgH₂ Nanoclusters within Nanoporous Aerogel Scaffold Materials. *ACS Nano* **2009**, *3*, 3521–3528.
- (12) Nielsen, T. K.; Bösenberg, U.; Gosalawit, R.; Dornheim, M.; Cerenius, Y.; Besenbacher, F.; Jensen, T. R. A Reversible Nanoconfined Chemical Reaction. *ACS Nano* **2010**, *4*, 3903–3908.
- (13) Gosalawit-Utke, R.; Milanese, C.; Nielsen, T. K.; Karimi, F.; Saldan, I.; Pranzas, K.; Jensen, T. R.; Marini, A.; Klassen, T.; Dornheim, M. Nanoconfined 2LiBH₄–MgH₂ for Reversible Hydrogen Storages: Reaction Mechanisms, Kinetics and Thermodynamics. *Int. J. Hydrogen Energy* **2013**, *38*, 1932–1942.
- (14) Stephens, R. D.; Gross, A. F.; Van Atta, S. L.; Vajo, J. J.; Pinkerton, F. E. The Kinetic Enhancement of Hydrogen Cycling in NaAlH₄ by Melt Infusion into Nanoporous Carbon Aerogel. *Nanotechnology* **2009**, *20*, No. 204018.
- (15) Nielsen, T. K.; Javadian, P.; Polanski, M.; Besenbacher, F.; Bystrzycki, J.; Jensen, T. R. Nanoconfined NaAlH₄: Determination of Distinct Prolific Effects from Pore Size, Crystallite Size, and Surface Interactions. *J. Phys. Chem. C* **2012**, *116*, 21046–21051.
- (16) Nielsen, T. K.; Javadian, P.; Polanski, M.; Besenbacher, F.; Bystrzycki, J.; Skibsted, J.; Jensen, T. R. Nanoconfined NaAlH₄: Prolific Effects from Increased Surface Area and Pore Volume. *Nanoscale* **2014**, *6*, 599–607.
- (17) Lin, C.; Ritter, J. A. Carbonization and Activation of Sol-gel Derived Carbon Xerogels. *Carbon* **2000**, *38*, 849–861.
- (18) Yu, Y.; Chen, C.-H.; Shui, J.-L.; Xie, S. Nickel-Foam-Supported Reticular CoO-Li₂O Composite Anode Materials for Lithium Ion Batteries. *Angew. Chem., Int. Ed.* **2005**, *44*, 7085–7089.
- (19) Gu, W.; Magasinski, A.; Zdryko, B.; Yushin, G. Metal Fluorides Nanoconfined in Carbon Nanopores as Reversible High Capacity Cathodes for Li and Li-Ion Rechargeable Batteries: FeF₂ as an Example. *Adv. Energy Mater.* **2015**, *5*, No. 1401148.
- (20) Marino, C.; Boulet, L.; Gaveau, P.; Fraisse, B.; Monconduit, L. Nanoconfined Phosphorus in Mesoporous Carbon as an Electrode for Li-Ion Batteries: Performance and Mechanism. *J. Mater. Chem.* **2012**, *22*, 22713.
- (21) Oumella, Y.; Zlotea, C.; Bastide, S.; Cachet-Vivier, C.; Léonel, E.; Sengmany, S.; Leroy, E.; Aymard, L.; Bonnet, J.-P.; Latroche, M. Bottom-up Preparation of MgH₂ Nanoparticles with Enhanced Cycle Life Stability during Electrochemical Conversion in Li-Ion Batteries. *Nanoscale* **2014**, *6*, 14459–14466.
- (22) Hao, F.; Zhang, Z.; Yin, L. Co₃O₄/Carbon Aerogel Hybrids as Anode Materials for Lithium-Ion Batteries with Enhanced Electrochemical Properties. *ACS Appl. Mater. Interfaces* **2013**, *5*, 8337–8344.
- (23) Liu, N.; Shen, J.; Liu, D. A Fe₂O₃ Nanoparticle/Carbon Aerogel Composite for Use as an Anode Material for Lithium Ion Batteries. *Electrochim. Acta* **2013**, *97*, 271–277.
- (24) Ji, X.; Lee, K. T.; Nazar, L. F. A Highly Ordered Nanostructured Carbon–sulphur Cathode for Lithium–sulphur Batteries. *Nat. Mater.* **2009**, *8*, 500–506.
- (25) Shen, L.; Zhang, X.; Uchaker, E.; Yuan, C.; Cao, G. Li₄Ti₅O₁₂ Nanoparticles Embedded in a Mesoporous Carbon Matrix as a Superior Anode Material for High Rate Lithium Ion Batteries. *Adv. Energy Mater.* **2012**, *2*, 691–698.
- (26) Wang, G.; Liu, H.; Liu, J.; Qiao, S.; Lu, G. M.; Munroe, P.; Ahn, H. Mesoporous LiFePO₄/C Nanocomposite Cathode Materials for High Power Lithium Ion Batteries with Superior Performance. *Adv. Mater.* **2010**, *22*, 4944–4948.
- (27) Al-Muhtaseb, S. A.; Ritter, J. A. Preparation and Properties of Resorcinol-Formaldehyde Organic and Carbon Gels. *Adv. Mater.* **2003**, *15*, 101–114.
- (28) Zheng, T.; Xue, J. S.; Dahn, J. R. Lithium Insertion in Hydrogen-Containing Carbonaceous Materials. *Chem. Mater.* **1996**, *8*, 389–393.
- (29) Winter, M.; Besenhard, J. O.; Spahr, M. E.; Novák, P. Insertion Electrode Materials for Rechargeable Lithium Batteries. *Adv. Mater.* **1998**, *10*, 725–763.
- (30) Fichtner, M. Nanoconfinement Effects in Energy Storage Materials. *Phys. Chem. Chem. Phys.* **2011**, *13*, 21186.
- (31) Lee, B.-M.; Jang, J.-W.; Shim, J.-H.; Cho, Y. W.; Lee, B.-J. Thermodynamic Assessment of the NaH ↔ Na₃AlH₆ ↔ NaAlH₄ Hydride System. *J. Alloys Compd.* **2006**, *424*, 370–375.
- (32) An, S. J.; Li, J.; Daniel, C.; Mohanty, D.; Nagpure, S.; Wood, D. L. The State of Understanding of the Lithium-Ion-Battery Graphite Solid Electrolyte Interphase (SEI) and Its Relationship to Formation Cycling. *Carbon* **2016**, *105*, 52–76.
- (33) Zhou, H.; Zhu, S.; Hibino, M.; Honma, I.; Ichihara, M. Lithium Storage in Ordered Mesoporous Carbon (CMK-3) with High Reversible Specific Energy Capacity and Good Cycling Performance. *Adv. Mater.* **2003**, *15*, 2107–2111.
- (34) Hu, Y.-S.; Adelhelm, P.; Smarsly, B. M.; Hore, S.; Antonietti, M.; Maier, J. Synthesis of Hierarchically Porous Carbon Monoliths with Highly Ordered Microstructure and Their Application in Rechargeable Lithium Batteries with High-Rate Capability. *Adv. Funct. Mater.* **2007**, *17*, 1873–1878.
- (35) Kaskhedikar, N. A.; Maier, J. Lithium Storage in Carbon Nanostructures. *Adv. Mater.* **2009**, *21*, 2664–2680.
- (36) Hudak, N.; Huber, D. Nanostructured Lithium-Aluminum Alloy Electrodes for Lithium-Ion Batteries. *ECS Trans.* **2011**, *33*, 1–13.
- (37) Hamon, Y.; Brousse, T.; Jousse, F.; Topart, P.; Buvat, P.; Schleich, D. M. Aluminum Negative Electrode in Lithium Ion Batteries. *J. Power Sources* **2001**, *97*–98, 185–187.
- (38) Tarascon, J. M.; Armand, M. Issues and Challenges Facing Rechargeable Lithium Batteries. *Nature* **2001**, *414*, 359–367.
- (39) Li, W.-C.; Lu, A.-H.; Weidenthaler, C.; Schüth, F. Hard-Templating Pathway To Create Mesoporous Magnesium Oxide. *Chem. Mater.* **2004**, *16*, 5676–5681.
- (40) Ryoo, R.; Joo, S. H.; Jun, S. Synthesis of Highly Ordered Carbon Molecular Sieves via Template-Mediated Structural Transformation. *J. Phys. Chem. B* **1999**, *103*, 7743–7746.
- (41) Zhao, D.; Feng, J.; Huo, Q.; Melosh, N.; Fredrickson, G. H.; Chmelka, B. F.; Stucky, G. D. Triblock Copolymer Syntheses of Mesoporous Silica with Periodic 50 to 300 Angstrom Pores. *Science* **1998**, *279*, 548–552.
- (42) Borkiewicz, O. J.; Shyam, B.; Wiaderek, K. M.; Kurtz, C.; Chupas, P. J.; Chapman, K. W. The AMPIX Electrochemical Cell: A Versatile Apparatus for in Situ X-Ray Scattering and Spectroscopic Measurements. *J. Appl. Crystallogr.* **2012**, *45*, 1261–1269.

(43) Hammersley, A. P.; Svensson, S. O.; Hanfland, M.; Fitch, A. N.; Hausermann, D. Two-Dimensional Detector Software: From Real Detector to Idealised Image or Two-Theta Scan. *High Pressure Res.* **1996**, *14*, 235–248.

(44) Rodríguez-Carvajal, J. Recent Advances in Magnetic Structure Determination by Neutron Powder Diffraction. *Phys. B* **1993**, *192*, 55–69.